

Fast Gradient Non-sign Methods

Yaya Cheng, Xiaosu Zhu, Qilong Zhang, Lianli Gao, Jingkuan Song[✉]

yaya.cheng@hotmail.com, xiaosu.zhu@outlook.com, qilong.zhang@std.uestc.edu.cn, jingkuan.song@gmail.com

ABSTRACT

Adversarial attacks make their success in “fooling” DNNs and among them, gradient-based algorithms become one of the main-streams. Based on the linearity hypothesis [12], under ℓ_∞ constraint, *sign* operation applied to the gradients is a good choice for generating perturbations. However, the side-effect from such operation exists since it leads to the bias of direction between the real gradients and the perturbations. In other words, current methods contain a gap between real gradients and actual noises, which leads to biased and inefficient attacks. Therefore in this paper, based on the Taylor expansion, the bias is analyzed theoretically and the correction of sign, *i.e.*, Fast Gradient Non-sign Method (FGNM), is further proposed. Notably, FGNM is a general routine, which can seamlessly replace the conventional *sign* operation in gradient-based attacks with negligible extra computational cost. Extensive experiments demonstrate the effectiveness of our methods. Specifically, ours outperform them by 27.5% at most and 9.5% on average. Our anonymous code is publicly available: <https://github.com/yaya-cheng/FGNM>.

CCS CONCEPTS

• Security and privacy → Human and societal aspects of security and privacy; • Computing methodologies → Machine learning;

KEYWORDS

Adversarial Attack, Taylor expansion, Gradient-based Methods

1 INTRODUCTION

Researchers have noticed that, by applying human-imperceptible perturbations, some “special” inputs will lead DNNs to give unreasonable outputs, which facilitates the born of adversarial attacks [5–7, 11, 12, 20–22, 42, 43, 45]. Although a series of DNNs have shown their incredible performance in computer vision tasks, the vulnerability of them is still a severe problem as their explosive development in recent years. Due to the fact that [10, 17, 18, 25, 28, 34, 44] have already revealed the potential security problems of DNNs, it is vital to learn to generate adversarial examples since it can help to evaluate and improve the robustness.

Several methods have been proposed to craft adversarial examples. In general, adversarial attacks can be grouped into two categories: Non-targeted attacks and targeted attacks. For targeted attacks, adversaries should induce the victim’s models to output specific wrong label. For non-targeted attacks, adversarial example is expected to mislead the victim’s models to output an arbitrary class except the original one. As a popular branch both in targeted and non-targeted attacks, gradient-based methods focus on how to produce proper perturbations based on gradients, such as one-step attacks [7, 12] and iterative-step attacks [6, 20, 43]. By taking the ascending direction of the gradient of objective function \mathcal{L} , *e.g.*,

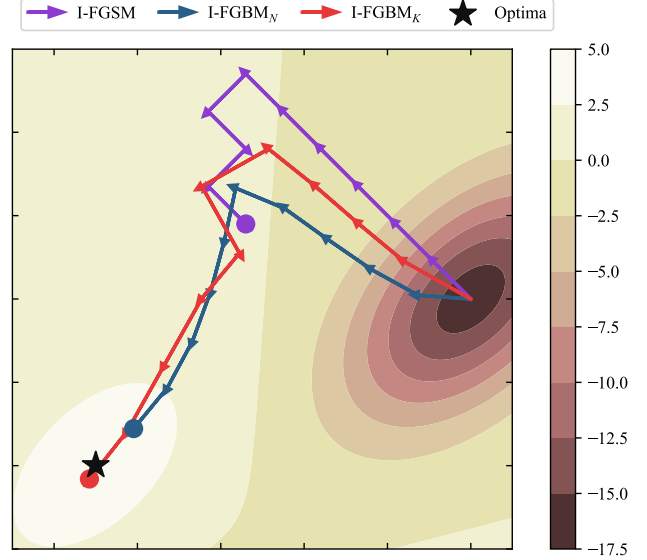


Figure 1: Visualization on a toy example of climbing the mountain with the traditional I-FGSM and our I-FGSM variants. Specifically, when adopting I-FGSM, the trajectory is biased due to the limitation of sign. It can not approach the optima and results in oscillation. Our I-FGSM_N holds the identical step size with I-FGSM in each iteration, but produces more precise trajectory and is therefore close to the optima. The I-FGSM_K considers the trade-off between magnitude and precision in each step, and gives the best result.

cross-entropy, perturbations are obtained and therefore the adversarial examples are pulled away from the original decision boundary. To make adversarial examples further away from this decision boundary and reduce computational overhead, most gradient-based methods decide to craft adversarial examples by performing sign operations according to the linearity hypothesis [12].

However, does *sign* drive perturbations to the appropriate way? Probably not. Given typical attack method I-FGSM [20] as the baseline, in Figure 2 (a), we give a demonstration of the side-effect of sign in the 2D Euclidean space in the last step, where the origin O' of the coordinate is close to ℓ_∞ ϵ -ball. As shown in the figure, gradient \mathbf{g} is extracted as two orthogonal direction, \mathbf{u} and \mathbf{v} . Assuming original gradient is composed of $\mathbf{g} = 0.5\mathbf{u} + 0.1\mathbf{v}$. After sign, the value is exceptional modified to $\frac{\epsilon}{7}\mathbf{u} + \frac{\epsilon}{7}\mathbf{v}$, having the included angle $\angle\theta = 33.7^\circ$ between \mathbf{g} and $\text{sign}(\mathbf{g})$. Obviously, after *sign*, the direction of the perturbation is not strictly following the original gradient. Although *sign* produces more perturbations under the ℓ_∞ -norm scenario, it also introduces bias into the direction of \mathbf{g} . Since gradient is treated as the direction of fastest increase of \mathcal{L}

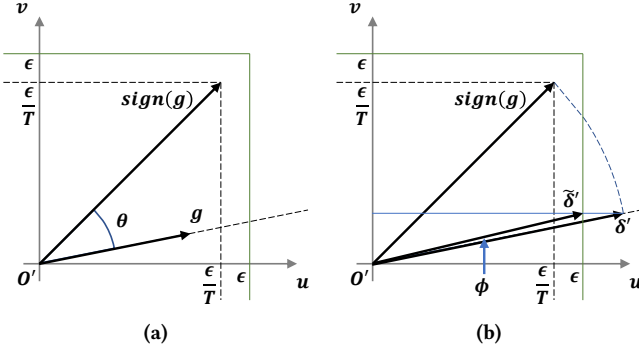


Figure 2: Demonstration of the side-effect of sign operation in the 2D Euclidean space in the last step. (a): After sign, there exist a included angle $\angle\theta$ between gradient g and $sign(g)$, (b): Our FGNM_N is done by firstly keeping magnitude same as $sign(g)$, directions same as g and then being clipped. Easily verified in the figure, the included angle ϕ between $\tilde{\delta}'$ and g is smaller than θ .

under the Euclidean feature space, the deviation in direction may make current gradient-based methods sub-optimal.

Therefore in this paper, we review the state-of-the-art attacks and give the correction on deviation in direction. Firstly, we introduce Taylor expansion to give a systematic analysis. Secondly, based on the analysis, our approach, Fast Gradient Non-sign Method is proposed, which completely replaces $sign$ with a refined one. Thirdly, by modifying the original algorithms as little as possible, such seamless replacement has been shown to provide a significant performance boosts on all methods in the exhaustive experiments. Figure 1 provides the toy example of climbing the mountain with three strategies to show the advantages of our FGNM. As demonstrated in the figure, noticed that the optima are inside the ϵ -ball, our two variants are easily to approach the optima. However, I-FGSM is stuck due to the distorted perturbations. Specifically, when adopting I-FGSM, the trajectory is biased due to the limitation of sign. It can not approach the optima and results in oscillation. Our I-FGNM_N holds the identical step size with I-FGSM in each iteration, but produces more precise trajectory and is therefore close to the optima. The I-FGNM_K considers the trade-off between magnitude and precision of perturbations in each step, and gives the best result.

Our contribution is summarized up as three folds:

- 1) Comprehensive analysis is conducted on the sign operation of gradient-based methods, which shows the bias between original gradients and the actual perturbations. As a result, this gap may hinder the abilities of current methods to maximize \mathcal{L} and therefore needs further correction.
- 2) A general and novel routine, Fast Gradient Non-sign Methods are proposed to correct the currently adopted sign routines. With comprehensive analysis, our methods are able to obtain less gap between gradients and actual perturbations than previous ones, which brings us ability to obtain performance boosts.
- 3) Extensive experiments reveal the effectiveness of our methods. Specifically, given the normally trained models as the black-box

models, ours outperform state-of-the-art attacks by 27.5% at most and 11.3% on average. When transferring our adversarial examples to defense models, we still achieve a noticeable performance gain (i.e., 25.8% at most and 7.0% on average).

2 RELATED WORKS

Adversarial attacks are a rising topic in recent advances of artificial intelligence. Although the neural networks go deeper and deeper, researchers find they are still vulnerable to specific inputs. In general, adversarial attacks can be classified into three categories: white-box, gray-box, and black-box attacks, which indicates how much information can we exploit from the victim’s models. White-box attacks have achieved noticeable attack performance since they are able to get all the information from the victim’s models [2, 32]. For gray-box attacks, adversaries can only access the output logits or predictions, adversarial examples are always crafted through huge amount queries [1, 33]. When all information from the victim’s models is unavailable, it becomes the most challenging black-box attacks and current methods always suffer from poor effectiveness. In our work, we mainly focus on black-box attacks.

2.1 Black-box Attacks.

Due to the fact that the decision boundaries of different models are similar, an important property of adversarial examples is their transferability, i.e., resultant adversarial examples generated from the white-box models are also effective for other models [27]. To tackle the poor performance of black-box attacks, several methods have been proposed to improve the transferability of adversarial examples [6, 7, 20, 21, 24, 43]. For example, Goodfellow *et al.* [12] propose the fast gradient sign method to craft adversarial examples with just one step. I-FGSM [20] extends FGSM to an iterative attack and further improves the performance of white-box attacks at the cost of transferability. To further improve the transferability, by creating diverse patterns, DI-FGSM finds adversarial examples which transfer better to black-box models. MI-FGSM [6] employs momentum term into the perturbation generation and achieve noticeable performance gains.

2.2 Defend against adversarial attacks.

The good transferability of adversarial examples enable black-box attacks feasible in physical world [3, 10, 16, 17, 19, 25, 29, 34, 35, 41]. Consequently, a variety of defense methods have been proposed to evade the threat of adversarial attacks [4, 8, 26, 30, 31, 39]. For example, Liu *et al.* perform defense by DNN bottleneck reinforcement scheme. Guo *et al.* preprocess adversarial examples before feeding them to the models by bit-depth reduction [23], JPEG compression [13], and image quilting [9]. Tramèr *et al.* propose ensemble adversarial training [40] to resist the adversarial perturbations and further improve the robustness of models.

3 METHODOLOGY

In this paper, we mainly discuss non-targeted attacks, and their targeted version can be simply derived. Formally, given arbitrary input image $x \in \mathbb{R}^{H \times W \times C}$ with ground-truth label y , non-targeted adversarial example x^{adv} aims at maximizing loss function $\mathcal{L}(x^{adv}, y)$

under the ℓ_p norm constraint:

$$\begin{aligned} \arg \max_{\mathbf{x}^{adv}} \mathcal{L}(\mathbf{x}^{adv}, y), \\ \text{s.t. } \|\mathbf{x}^{adv} - \mathbf{x}\|_p \leq \epsilon. \end{aligned} \quad (1)$$

To measure the human-imperceptibility of adversarial examples, we follow [6, 7, 43] and use ℓ_∞ -norm in our work. Specifically, when $p = \infty$, $\max|\mathbf{x}^{adv} - \mathbf{x}| \leq \epsilon$.

Some gradient-based attack methods [6, 7, 20] have been proposed to solve the optimization problem (1), e.g., I-FGSM performs T -step attack with a small step size $\alpha = \epsilon/T$:

$$\begin{aligned} \mathbf{x}_0^{adv} = \mathbf{x}, \mathbf{g}_t = \nabla_{\mathbf{x}_t^{adv}} \mathcal{L}(\mathbf{x}_t^{adv}, y), \\ \mathbf{x}_{t+1}^{adv} = \text{clip}_\epsilon^\mathbf{x}(\mathbf{x}_t^{adv} + \alpha \cdot \text{sign}(\mathbf{g}_t)), 0 \leq t < T, \end{aligned} \quad (2)$$

where sign operation makes perturbations meet the ℓ_∞ -norm bound as soon as possible, and clip operation is performed to make \mathbf{x}^{adv} satisfy the ϵ -ball of \mathbf{x} . Specifically:

$$\begin{aligned} \text{sign}(\cdot) = \begin{cases} +1 & \cdot > 0 \\ 0 & \cdot = 0 \\ -1 & \cdot < 0 \end{cases} \\ \text{clip}_\epsilon^\mathbf{x}(\cdot) = \min(\max(\cdot, \mathbf{x} - \epsilon), \mathbf{x} + \epsilon). \end{aligned} \quad (3)$$

Adopting the basic pipeline of I-FGSM, other iterative methods are arranged into similar formulations, where the basic idea is generalized: Performing method-specific manipulation on gradients \mathbf{g}_t and then generating the perturbations by sign operation.

3.1 Taylor Expansion of Loss Function.

To theoretically solve the optimization problem, i.e., Equation (1), we derive the first-order Taylor polynomial of \mathcal{L} at the point \mathbf{x}_{T-1}^{adv} as:

$$\begin{aligned} \mathcal{L}(\mathbf{x}_T^{adv}, y) &= \mathcal{L}(\mathbf{x}_{T-1}^{adv}, y) + (\mathbf{x}_T^{adv} - \mathbf{x}_{T-1}^{adv}) \cdot \nabla \mathcal{L}(\mathbf{x}_{T-1}^{adv}, y) + \mathcal{R}_1 \\ &= \mathcal{L}(\mathbf{x}, y) + \sum_{t=0}^{T-1} (\mathbf{x}_{t+1}^{adv} - \mathbf{x}_t^{adv}) \cdot \mathbf{g}_t + \mathcal{R}_1, \end{aligned} \quad (4)$$

where \mathcal{R}_1 is the remainder of first order and $\mathbf{g}_t = \nabla \mathcal{L}(\mathbf{x}_t^{adv}, y)$. Under the ℓ_∞ -norm constraint, we assume $\mathbf{x}_{t+1}^{adv} - \mathbf{x}_t^{adv}$ is so small that \mathcal{R}_1 can be neglected. By denoting $\mathbf{x}_{t+1}^{adv} - \mathbf{x}_t^{adv} = \delta_t$, Equation (4) is rewritten as:

$$\mathcal{L}(\mathbf{x}_T^{adv}, y) = \mathcal{L}(\mathbf{x}, y) + \sum_{t=0}^{T-1} \|\delta_t\| \|\mathbf{g}_t\| \cos \langle \delta_t, \mathbf{g}_t \rangle. \quad (5)$$

Obviously, $\sum_{t=0}^{T-1} \|\delta_t\| \|\mathbf{g}_t\| \cos \langle \delta_t, \mathbf{g}_t \rangle$ is the key component for maximizing $\mathcal{L}(\mathbf{x}_T^{adv}, y)$, where $\|\delta_t\|$ is the magnitude of i -th perturbation and $\langle \delta_t, \mathbf{g}_t \rangle$ is the included angle between δ_t and \mathbf{g}_t . Although $\|\mathbf{g}_t\|$ also affects the results, we treat it identical in different trajectories by assuming loss function is smooth and gradient does not change rapidly in a small region.

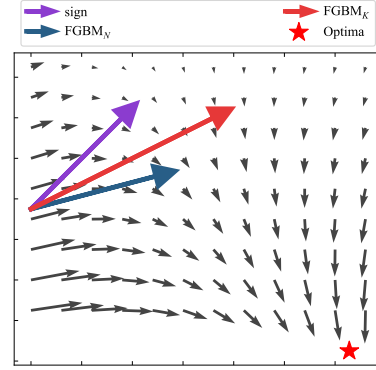


Figure 3: Quiver plot for visualizing gaps between original gradients and actual perturbations in the demo scenario. To approach optima in the fastest way, the magnitude and the direction of a step are both key components. In this figure, at the starting point, our FGSM_N and FGSM_K take the right step. However, the sign method goes far away instead.

3.2 Drawbacks of Sign-based Attacks

As mentioned above, \mathbf{g}_t indicates the direction of pulling \mathbf{x}_t^{adv} to increase \mathcal{L} . However, considering that sign simply quantifies gradients to $\{+1, -1, 0\}$, there always exists a bias of direction between the perturbation and gradients. As Figure 3 demonstrates, sign method pushes the point far away from the optima, which indicates the side-effect of this biased gradient manipulation. Based on the analysis in Sec. 3.1, in following sections we will explain why adopting sign will make Equation (5) sub-optimal and give our approach.

For simplicity, we hypothesize \mathbf{g}_t is non-zero. \mathbf{x}_t^{adv} and \mathbf{g}_t are interpreted as flattened vectors with dimension $D = H \times W \times C$:

$$\begin{aligned} \mathbf{x}_t^{adv} &= [x^1, x^2, \dots, x^D]_t, \\ \mathbf{g}_t &= [\nabla_{x^1}, \nabla_{x^2}, \dots, \nabla_{x^D}]_t. \end{aligned} \quad (6)$$

To make the derivation simple, we select the typical sign-based attack: I-FGSM as our baseline. Then, $\delta_t = \text{sign}(\mathbf{g}_t)$ and $\cos \langle \delta_t, \mathbf{g}_t \rangle$ is denoted as $\cos \theta_t$, where:

$$\cos \theta_t = \frac{\mathbf{g}_t \cdot \text{sign}(\mathbf{g}_t)}{\|\mathbf{g}_t\| \|\text{sign}(\mathbf{g}_t)\|} = \frac{\|\mathbf{g}_t\|_1}{\sqrt{\|\mathbf{g}_t\|_0} \|\mathbf{g}_t\|}. \quad (7)$$

Here, $\|\mathbf{g}_t\|_1 = \sum |\mathbf{g}_t^j|$, $\|\mathbf{g}_t\|_0 = D$. Due to the fact that $\|\cdot\|_1 \geq \|\cdot\|$ for any vector and $\|\cdot\|_1 = \|\cdot\|$ iff the vector is all zero or it only has one non-zero entry, $\cos \theta$ ranges in:

$$\frac{1}{\sqrt{D}} < \cos \theta \leq 1. \quad (8)$$

Obviously,

$$\|\delta_t\| = \alpha \sqrt{D} \quad (9)$$

$$\alpha < \|\delta_t\| \cos \theta \leq \alpha \sqrt{D}. \quad (10)$$

Two special cases will make $\cos \theta = 1$: a) $D = 1$, or b) All values of \mathbf{g}_t are identical, which makes $\|\mathbf{g}_t\|_1 = \sqrt{D} \|\mathbf{g}_t\|$.

The derivation of θ_t indicates the gap between real gradients and actual perturbations at current iteration i . In fact, special cases mentioned above are nearly impossible to approach in practice especially in high-dimensional space. Therefore the ideal maximum of $\|\delta_t\| \cos \theta_t$ is difficult to achieve, and we usually seek the sub-optimal solution of Equation (4).

3.3 Fast Gradient Non-sign Methods

3.3.1 Fixed Scale Approach. To reduce the side-effect caused by sign, Iterative Fast Gradient Non-sign Method (I-FGNM) and other variants are proposed. To distinguish our method, we denote the magnitude of our noise as $\|\delta'\|$ and the included angle as ϕ . An intuitive solution is to perform a linear scale on the \mathbf{g}_t so that $\|\delta'\| = \|\text{sign}(\mathbf{g}_t)\|$ and naturally $\cos \phi = 1 \geq \cos \theta$. To achieve this, a scale factor ζ is defined as:

$$\zeta = \frac{\|\text{sign}(\mathbf{g}_t)\|}{\|\mathbf{g}_t\|}, \quad \delta'_t = \alpha \cdot \zeta \cdot \mathbf{g}_t. \quad (11)$$

We call this simple solution as I-FGNM_N since the norm between δ' and $\text{sign}(\mathbf{g})$ are equal.

Empirically in iterative algorithms, the step size α are much smaller than ϵ . So in the first few steps, our noises are too small to be clipped. We have:

$$\|\delta_t\| \cos \theta_t \leq \|\delta'_t\| \cos \phi_t = \alpha \sqrt{D}. \quad (12)$$

The derivation shows that \mathcal{L} calculated from our approach will always be greater or equal than the sign approach, according to Equation (12) and (5) if there is no clipping. However, in the last few steps, the accumulated noises of previous steps make \mathbf{x}_t^{adv} close to the ϵ -ball, and it will be more likely to be clipped. In this scenario, the actual noises added in the t -th iteration will be:

$$\mathbf{x}_{t+1}^{adv} - \mathbf{x}_t^{adv} = \text{clip}_\epsilon^{\mathbf{x}} \left(\mathbf{x}_t^{adv} + \alpha \cdot \delta'_t \right) - \mathbf{x}_t^{adv}. \quad (13)$$

Clipping introduces biases, i.e., $\|\delta'_t\|$ decreases and $\cos \phi_t$ will be smaller than 1. It is complicated to judge the clipped δ'_t and δ_t which one is better. And instead, we analyze it in a qualitative way. The clipped δ'_t contains two parts: The non-clipped component and clipped component. If we only consider the non-clipped one, it still preserves the original gradients and performs linear scale. On the contrary, the clipped one only contains $-\epsilon$ or $+\epsilon$. So we treat it as **partially distorted**. Different from $\text{sign}(\mathbf{g}_t)$ which is **fully distorted**, our mixed vector is more likely to be closed to \mathbf{g}_t than $\text{sign}(\mathbf{g}_t)$. Figure 2 demonstrates the analysis on clipping. As the figure shows, the \mathbf{u} -component of δ' is reduced to ϵ while the \mathbf{v} -component of δ' is preserved. The actual perturbation is denoted as $\tilde{\delta}'$. Easily verified in the figure, the scaled and clipped result $\tilde{\delta}'$ is closer to \mathbf{g}_t . Overall, $\sum_{t=0}^T \|\tilde{\delta}'_t\| \cos \phi_t$ is larger than $\sum_{t=0}^T \|\delta_t\| \cos \theta_t$.

3.3.2 Adaptive Scale Approach. Although I-FGNM_N is applicable for most cases by fixing $\|\delta'_t\|$, the attack performance is not always guaranteed due to clipped ratio. Empirically, a large clipped ratio hinders the performance of I-FGNM_N. To consider this ratio formally and comprehensively, we relax the constraint on $\|\delta'_t\|$ and compose a heuristic method I-FGNM_K, where the scale factor of I-FGNM_K is set by directly finding the proper value from all possible

Algorithm 1: Algorithms of I-FGNM

Input : A classifier \mathcal{F} with loss function \mathcal{L} ; input image \mathbf{x} with ground-truth label y ; T iterations; the size of perturbation ϵ ;

Output : Adversarial example \mathbf{x}^{adv} with

$$\|\mathbf{x}^{adv} - \mathbf{x}\|_\infty \leq \epsilon;$$

1 Initialize: $\mathbf{x}_0^{adv} = \mathbf{x}$, $\alpha = \epsilon/T$

2 $t \leftarrow 0$;

3 **while** $t < T$ **do**

 /* generation loop of \mathbf{x}^{adv} */

4 Input \mathbf{x}_t^{adv} to \mathcal{L} and obtain the gradient

$$\mathbf{g}_t = \nabla_{\mathbf{x}} \mathcal{L}(\mathbf{x}_t^{adv}, y);$$

5 Calculate ζ by Equation (11) or Equation (14);

6 Update \mathbf{x}_{t+1}^{adv} by our non-sign operation as

$$\mathbf{x}_{t+1}^{adv} = \mathbf{x}_t^{adv} + \alpha \cdot \zeta \cdot \mathbf{g}_t;$$

7 $t \leftarrow t + 1$;

8 **end**

values:

$$\begin{aligned} \text{scales} &= \text{Sort} \left(\frac{1}{\|\mathbf{g}_t^k\|} \right), \quad \mathbf{g}_t^k \in \mathbf{g}_t, \\ \zeta &= \text{scales}[K]. \end{aligned} \quad (14)$$

Specifically, *scales* are calculated and sorted from $1/\|\mathbf{g}_t^k\|$, then ζ is picked by the K -th *biggest* value of *scales*. As described before, two components (magnitude and direction of noise) essentially influence the attack performance. For I-FGNM_K, there exists a trade-off between the two components, which is influenced by controlling K . Intuitively, larger K leads to smaller magnitude of noises, smaller clipped ratio, and larger $\cos \phi_t$. The Fast Gradient Non-sign Methods is summarized in Algorithm 1.

3.4 Discussion

Our Fast Gradient Non-sign Methods are delivered with two variants, FGNM_N and FGNM_K. The former generates noises δ' by linearly scaling from \mathbf{g} and keeping the magnitude same as $\|\text{sign}(\mathbf{g}_t)\|$ with a scale ζ . The latter relaxes the magnitude to consider the trade-off between $\|\delta'\|$ and $\cos \phi$. Moreover, the replacement is seamless and universal so that any current FGSM-based attacks are applicable to become FGNM-based attacks, e.g., MI-FGSM, TI-FGSM, DI-FGSM, SI-FGSM, and the computational overhead is negligible.

Noticed that there also exists another style of attack whose constraint is defined as $\|\mathbf{x}^{adv} - \mathbf{x}\| \leq \epsilon$ (ℓ_2 attacks). We need to clarify the difference between our FGNM and ℓ_2 attacks. Firstly, since the constraint is changed, ℓ_2 attacks are not troubled by the ℓ_∞ constraint which causes the gradients to be distorted. Secondly, our approaches essentially consider the way to reduce the side-effect of sign operation to finally leverage the performance of ℓ_∞ attacks. Therefore, we believe our approaches have advantages among the ℓ_∞ attacks.

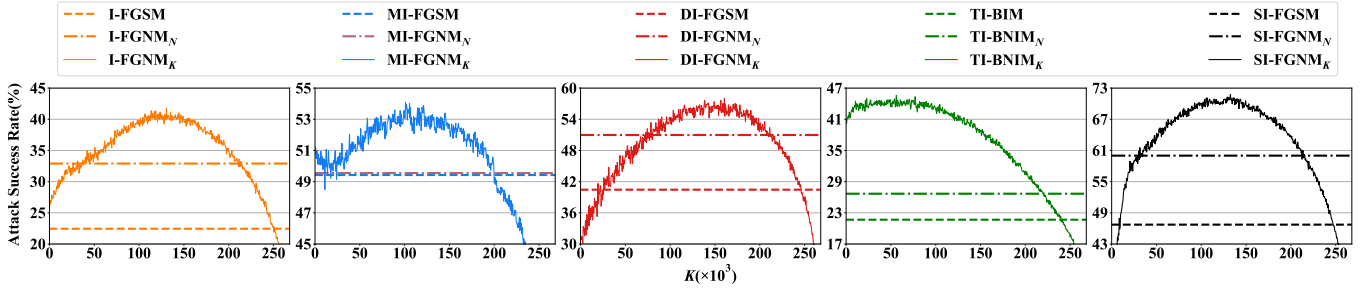


Figure 4: Average attack success rate comparisons between sign methods and our FGSM_K variants on NT. We employ Inc-v3 as white-box and compute average attack success rate of other four black-box models (Inc-v4, Res152, IncRes, and Den161) w.r.t. K . Results of sign-based methods and FGSM_N variants are also reported as dashed lines and dash-dotted lines, respectively.

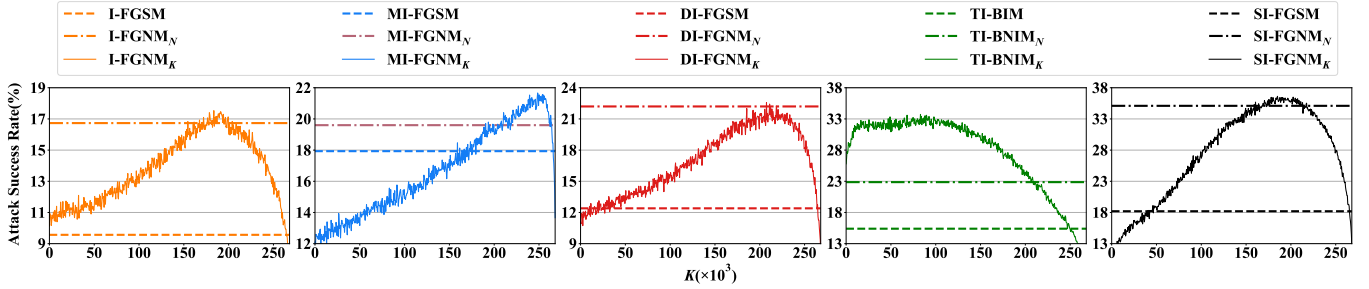


Figure 5: Average attack success rate comparisons between sign methods and our FGSM_K variants on EAT. We employ Inc-v3 as white-box and compute average attack success rate of three black-box models (Inc-v3_{ens3}, Inc-v3_{ens4}, IncRes_{ens}) w.r.t. K . Different from NT, the best results present in the later area in most cases. Results of sign-based methods and FGSM_N variants are also reported as dashed lines and dash-dotted lines, respectively.

4 EXPERIMENTS

To confirm our analysis and compare with currently state-of-the-art attacks, extensive experiments are conducted in the non-targeted ℓ_∞ attack scenario.

4.1 Setup

Dataset. The ImageNet-compatible dataset in the NIPS 2017 adversarial competition¹ is chosen to evaluate our methods and state-of-the-art attacks. This dataset contains 1,000 images and is widely used in previous works [6, 7, 11, 24].

Models. To give a comprehensive statistical analysis, experiments are conducted on eight models, including five normally trained models (NT): Inception V3 (Inc-v3) [38], Inception V4 (Inc-v4) [36], ResNet152 V2 (Res152) [14], Inception-Resnet V2 (IncRes) [37] and DenseNet 161 (Den161) [15], and three ensemble adversarially trained models (EAT): Inception V3 (Inc-v3) [38], Inception V4 (Inc-v4) [36], ResNet152 V2 (Res152) [14], Inception-Resnet V2 (IncRes) [37] and DenseNet 161 (Den161) [15] are NT, and for EAT (defense models), Inc-v3_{ens3}, Inc-v3_{ens4} and IncRes_{ens} [40] are employed. The experiments are conducted in a white-box \rightarrow black-box fashion.

Baselines. As described above, our two solutions are applicable for any FGSM-based methods by directly replacing sign with scale ζ . In this paper, five currently popular FGSM-based attacks are

Table 1: Hyper-parameters adopted in our experiments for MI-FGSM, DI-FGSM, TI-BIM and SI-FGSM respectively. For a fair comparison, our methods use identical hyper-parameters.

Methods	Hyper-parameters	Value
MI-FGSM	Momentum μ	1.0
DI-FGSM	Transform probability p	0.7
TI-BIM	Kernel length W	15
SI-FGSM	Number of the scale copies c	5

selected as baselines: I-FGSM [20], MI-FGSM [6], DI-FGSM [43], TI-BIM [7] and SI-FGSM [24]. Our boosted versions are denoted as I-FGSM, MI-FGSM, DI-FGSM, TI-BIM, SI-FGSM, respectively. Both of the two versions (FGSM_N and FGSM_K) are evaluated.

Hyper-parameters. To make a fair comparison, we follow the previous works [6, 7, 24, 43] to set hyper-parameters. For the generalized parameters, we set $\epsilon = 16$ with pixel level ranges in $0 \sim 255$. And for iterative methods, their iteration count are $T = 10$ identically, step size α is therefore $\epsilon/T = 1.6$. As for method-specific hyper-parameters, we adopt the original value reported in their paper, as shown in Table 1. Note that our methods will not modify these hyper-parameters.

¹<https://www.kaggle.com/c/nips-2017-non-targeted-adversarial-attack>

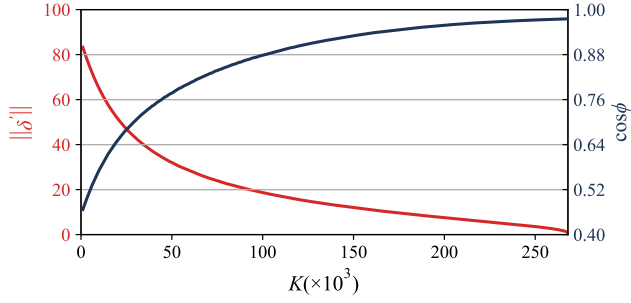


Figure 6: Evaluation on average $\cos \phi$ and $\|\delta'\|$ w.r.t. K to show the changes of magnitude and direction of added perturbations. Obviously, $\|\delta'\|$ decreases when K increases, and $\cos \phi$ goes up in contrast. The trends confirm our analysis about magnitude and direction of noises.

4.2 Effectiveness of K .

In this section, we firstly study the effectiveness of K since it represents the trade-off between magnitude and bias of noises.

To find an appropriate K , given Inc-v3 as white-box models and K ranging from 1 to $299 \times 299 \times 3$ with interval 500, we firstly craft adversarial examples using all FGNM_K-based methods and then report the average attack success rate against black-box NT and EAT in Figure 4 and Figure 5 respectively. We also plot the performance of sign-based methods and our FGNM_N methods, which will be discussed in next sections. As demonstrated from the convex curves in Figure 4 and Figure 5. As for NT, we give a unified optimal K for all methods $k = 120,000$. For EAT, $k = 200,000$.

A natural question is that why the attack performance curves in Figure 4 and Figure 5 are convex. Given that the attack performance trends do not change with different FGNM_K methods in Figure 4 and Figure 5, we only consider I-FGNM_K to answer this question. As described before, the magnitude and bias of noises plays a key role in performing successful attack. Therefore, a potential reason for the convex trends is the analysis of these two components in Sec 3.3.1. To confirm the analysis in Sec 3.3.1, we measure these two values on I-FGNM_K. To obtain actual noises added in the i -th iteration, we compute $\delta'_i = \mathbf{x}_{t+1}^{adv} - \mathbf{x}_t^{adv}$. Then, magnitude is computed by $\|\delta'_i\|$ and bias of direction is computed by $\cos \phi_t = \frac{\langle \delta'_i, \mathbf{g}_t \rangle}{\|\delta'_i\| \|\mathbf{g}_t\|}$ and they are averaged among whole iterations. The results with respect to K are placed in Figure 6. This figure shows our idea for presenting the trends of $\|\delta'\|$ and $\cos \phi$ when varying K . Particularly, when K increases, the scale ζ decreases, and therefore the generated perturbations will be smaller. Meanwhile, smaller perturbations leads to a smaller clipped ratio, and instead preserves the direction. So the actual $\|\delta'\|$ goes down while $\cos \phi$ goes up. Naturally, there exists a maximum value of $\|\delta'\| \cos \phi$.

4.3 Comparisons with State-of-the-Art Attacks

After finding the optimal K , comprehensive experiments are conducted to further evaluate the effectiveness of our methods against NT and EAT.

4.3.1 Attack against Normally Trained Models. In this section, we study the vulnerability of NT w.r.t different algorithms, including FGNM_N-based, FGNM_K-based and their corresponding FGSM-based methods. Adversarial examples are crafted via given white-box models by different methods.

As shown in Table 2, FGNM_N and FGNM_K sustain powerful white-box attack performance since they achieve near 100% success rate against all white-box models. For black-box attacks, our methods are applicable to most attacks, such as I-FGSM, DI-FGSM, TI-BIM, SI-FGSM. Specifically, by integrating FGNM_N with them, our methods surpass I-FGSM, DI-FGSM, TI-BIM, SIFGSM in the black-box manner by a large margin, i.e., on average, **9.8%**, **8.6%**, **6.8%**, **11.4%** respectively. For MI-FGNM_N which is based on cumulative gradients, the gradients are so large that most of the pixels will be clipped if applying FGNM_N to them, and therefore no noticeable performance leverage is obtained by MI-FGNM_N compared with MI-FGSM. By intergrating FGNM_K with each FGSM-based method, our methods outperform I-FGSM, MI-FGSM, DI-FGSM, TI-BIM, SI-FGSM for the black-box attacks by **18.7%**, **3.3%**, **14.1%**, **20.3%**, **20.7%**.

4.3.2 Attack against Defense Models. Adversarial training technique is an effective way to evade attacks, especially for black-box attacks. However, we still obtain the expected results. As placed in Table 3, our FGNM_N and FGNM_K achieve the best performance in most cases, especially for I-FGNM_K, MI-FGNM_N, DI-FGNM_N, TI-BNIM_K, and SI-FGNM_K, which outperform their baselines by **12.0%**, **17.2%**, **13.3%** and **26.4%** on average. Results among MI variants are also satisfied, where our MI-FGNM_N obtain **4.2%** performance gain on average.

It is noticeable that our FGNM_N approaches have smaller performance gap with our FGNM_K approaches on EAT than NT. We also observe different performance trends w.r.t. K for two kinds of models in Figure 4 and 5, which indicates the way EAT perceive images is different. It is worth discussing in future works.

4.3.3 Effectiveness on Combination of Methods. To further verify the effectiveness of our methods, we also report the results on different combination of methods. Specially, four combinations are selected: DTI-FGSM, DSI-FGSM, DTSI-FGSM, MDTSI-FGSM. Given Inc-v3 as the white-box model, adversarial examples are crafted by these four attacks and their FGNM_N and FGNM_K variants. As demonstrated in Table. 4, when the victim's model is in NT, noticeable performance gain is achieved by just applying our FGNM_N to them. The most powerful attacks come from FGNM_K variants, which outperform state-of-the-art attacks by **21.9%** at most and **11.7%** on average. For EAT, FGNM_K variants achieves comparable results of FGNM_N variants, which outperforms state-of-the-art attacks by **23.1%** at most and **10.5%** on average.

4.4 Analysis

4.4.1 Analysis of MI-FGSM. From the experimental results, we observe that the performance gain on MI-FGNM_N is not significant compared with other methods. A potential reason is that MI-FGSM applies momentum term to the perturbations generation. The accumulated noises lead to larger clipped ratio than other methods and hinder the performance of MI-FGNM_N. Further experiments

Table 2: Quantitative comparisons between state-of-the-art attacks on NT. Specifically, Inc-v3, Inc-v4, Res152 and IncRes are adopted to craft adversarial examples respectively. “*” denotes the white-box results while others are black-box results.

Models	Attacks	Inc-v3	Inc-v4	Res152	IncRes	Den161	Models	Inc-v3	Inc-v4	Res152	IncRes	Den161
Inc-v3	I-FGSM	100.0*	29.4	18.9	20.3	21.2	Inc-v4	42.0	100.0*	22.6	25.8	24.4
	I-FGSM _N	100.0*	41.9	28.2	33.4	28.1		51.5	100.0*	32.2	35.5	31.0
	I-FGSM _K	100.0*	48.7	32.7	44.2	36.5		63.0	100.0*	40.4	46.0	44.3
	MI-FGSM	100.0*	55.1	43.0	50.9	48.7		70.8	100.0*	52.2	59.0	55.5
	MI-FGSM _N	100.0*	56.2	42.8	52.3	46.9		69.7	100.0*	50.0	58.2	52.3
	MI-FGSM _K	100.0*	59.0	45.9	57.9	51.1		74.3	100.0*	54.0	63.3	56.5
	DI-FGSM	99.9*	54.9	33.6	41.7	31.6		64.9	100.0*	39.1	49.4	37.2
	DI-FGSM _N	99.7*	65.3	43.7	55.1	39.8		73.7	100.0*	47.8	59.4	45.2
	DI-FGSM _K	100.0*	67.3	45.6	62.0	47.0		78.4	100.0*	55.0	66.4	54.5
	TI-BIM	99.9*	28.1	16.7	13.5	28.4		35.2	100.0*	20.4	17.0	31.8
	TI-BNIM _N	100.0*	25.9	23.3	23.9	33.6		46.3	100.0*	27.4	26.7	40.2
	TI-BNIM _K	100.0*	47.4	33.6	35.9	47.6		58.2	100.0*	35.6	39.4	54.7
Res152	SI-FGSM	99.0*	53.8	40.4	47.8	44.9	IncRes	72.6	100.0*	51.0	57.0	57.2
	SI-FGSM _N	99.0*	67.7	52.7	63.2	56.4		78.0	100.0*	61.3	70.8	65.1
	SI-FGSM _K	99.0*	76.6	64.1	73.2	67.0		86.4	100.0*	71.9	77.9	76.6
	I-FGSM	31.4	25.1	99.5*	17.0	23.8		46.2	38.6	27.6	100.0*	28.1
	I-FGSM _N	40.8	35.3	99.1*	30.5	34.3		56.6	49.3	35.7	99.9*	35.8
	I-FGSM _K	52.0	46.6	99.5*	42.4	44.9		65.6	53.8	39.0	100.0*	43.5
	MI-FGSM	56.1	50.8	99.5*	47.2	54.6		76.4	67.8	57.0	100.0*	60.3
	MI-FGSM _N	55.7	49.6	99.5*	46.2	52.7		75.2	65.6	55.2	100.0*	58.3
	MI-FGSM _K	62.6	56.7	99.5*	53.9	58.0		77.0	69.2	58.6	100.0*	61.2
	DI-FGSM	62.1	55.6	99.1*	49.4	47.4		70.6	66.7	48.1	99.5*	45.1
	DI-FGSM _N	69.9	64.2	99.3*	58.7	56.5		76.9	74.3	56.3	99.6*	51.9
	DI-FGSM _K	76.2	70.1	99.6*	67.1	64.8		80.6	76.8	56.8	98.8*	57.8
	TI-BIM	24.7	21.3	99.2*	11.5	30.9		44.0	40.2	26.3	99.4*	41.0
Inc-v3	TI-BNIM _N	33.1	27.8	99.0*	19.1	35.9	Inc-v4	51.0	45.4	30.5	99.6*	46.5
	TI-BNIM _K	47.0	41.6	99.5*	33.3	54.2		63.0	56.5	43.1	99.0*	61.6
	SI-FGSM	43.6	40.0	99.8*	30.6	44.6		72.8	63.9	52.7	99.9*	58.8
	SI-FGSM _N	53.9	48.9	99.7*	53.9	56.3		81.3	73.5	64.6	99.9*	67.7
	SI-FGSM _K	66.0	62.6	99.8*	58.1	68.6		86.6	80.6	70.7	100.0*	75.4

Table 3: Quantitative comparisons between state-of-the-art attacks on EAT. Inc-v3, Inc-v4, Res152 and IncRes are adopted as white-box models to generate adversarial examples respectively, while EAT are used to test transferability.

Attacks	Inc-v3			Inc-v4			Res152			IncRes		
	Inc-v3 _{ens3}	Inc-v3 _{ens4}	IncRes _{ens}	Inc-v3 _{ens3}	Inc-v3 _{ens4}	IncRes _{ens}	Inc-v3 _{ens3}	Inc-v3 _{ens4}	IncRes _{ens}	Inc-v3 _{ens3}	Inc-v3 _{ens4}	IncRes _{ens}
I-FGSM	12.1	12.6	4.6	12.0	12.0	5.8	12.3	13.4	6.7	13.3	12.8	8.9
I-FGSM _N	18.9	20.8	10.5	18.7	19.5	11.6	21.7	22.5	15.5	26.2	23.8	18.4
I-FGSM _K	18.5	20.1	10.6	19.9	20.7	12.2	22.4	23.9	16.1	26.3	24.2	19.2
MI-FGSM	22.2	21.2	10.4	24.6	22.4	13.4	24.7	26.7	15.7	31.2	28.6	20.7
MI-FGSM _N	22.8	23.2	12.8	26.3	26.4	16.1	31.0	30.0	19.0	36.5	32.1	25.7
MI-FGSM _K	21.9	23.3	11.9	25.3	25.2	14.7	31.2	28.7	18.4	34.6	31.5	23.0
DI-FGSM	14.2	15.7	7.3	14.6	16.8	9.4	21.0	20.9	12.4	20.8	18.7	12.3
DI-FGSM _N	24.7	27.0	14.9	27.3	26.0	17.1	38.1	36.2	26.4	38.3	34.7	28.5
DI-FGSM _K	24.3	26.7	13.4	27.0	26.7	17.3	37.7	35.1	26.6	37.8	35.0	27.1
TI-BIM	17.5	18.0	10.7	17.2	20.4	11.8	18.5	18.7	12.6	25.4	25.8	21.1
TI-BNIM _N	25.6	25.9	17.1	28.5	28.3	19.8	25.3	25.4	19.7	37.4	35.9	30.6
TI-BNIM _K	27.3	27.3	18.8	29.1	28.4	20.4	27.9	29.0	21.3	37.7	37.0	33.8
SI-FGSM	21.7	22.5	10.4	27.3	28.5	16.9	20.2	18.7	12.3	30.0	28.2	21.6
SI-FGSM _N	38.8	41.1	25.4	49.6	48.5	33.2	37.0	34.6	27.3	54.3	48.3	45.7
SI-FGSM _K	40.0	42.4	25.3	50.9	49.0	32.2	37.9	37.8	27.4	55.8	50.5	46.4

are conducted to verify this. Given Inc-v3 as the white-box model, we report the magnitude of noises before clipping over the whole dataset at iteration 2, 5, and 10 using various methods, including I-FGSM_N, I-FGSM_K, MI-FGSM_N, MI-FGSM_K. As demonstrated in Figure 7, the clipped ratio of I-FGSM_N at iteration 2, 5, and 10 is 0.07%, 0.03% and 0.8% respectively. For I-FGSM_K, it is 0.2%, 0.8%, and 1.5%. For MI-FGSM_N, it is 0.2%, 3.7%, 15%. For MI-FGSM_K,

it is 0.6%, 3.5%, 7.6%. In brief, no more than 0.8% of perturbations in I-FGSM_N will be clipped, but for MI-FGSM_N, the percentage increases to 15.0%. The larger clipped ratio distorts the direction of perturbations and decrease the magnitude of the final noise, which further hinders performance of MI-FGSM_N. Different from MI-FGSM_N, MI-FGSM_K considers the trade-off between magnitude and bias to increase performance.

Table 4: Quantitative comparisons between different combinations of methods. Adversarial examples are crafted via Inc-v3, then Inc-v4, Res152, IncRes, Den161, In-v3_{ens3}, Inc-v3_{ens4} and IncRes_{ens} are used to test the transferability.

Attacks	Inc-v3	Inc-v4	Res152	IncRes	Den161	Inc-v3 _{ens3}	Inc-v3 _{ens4}	IncRes _{ens}
DTI-FGSM	98.6*	46.2	25.0	27.4	41.0	24.0	26.8	15.1
DTI-FGSM _N	98.9*	53.4	32.7	37.4	47.8	35.4	36.0	24.2
DTI-FGSM _K	99.8*	63.6	42.1	49.3	61.1	38.8	38.3	25.9
DSI-FGSM	100.0*	82.7	67.5	76.0	72.1	32.9	32.6	17.3
DSI-FGSM _N	100.0*	86.9	75.0	83.3	78.7	55.7	55.7	37.4
DSI-FGSM _K	100.0*	91.4	78.7	88.6	83.0	53.2	54.5	35.7
DTSI-FGSM	99.5*	69.8	49.0	54.1	74.4	49.8	50.6	35.6
DTSI-FGSM _N	99.8*	74.8	52.3	60.8	78.6	58.7	60.4	43.8
DTSI-FGSM _K	100.0*	81.5	62.3	68.4	85.6	60.6	63.0	47.6
MDTSI-FGSM	99.4*	75.5	59.6	62.0	82.9	67.9	69.2	53.4
MDTSI-FGSM _N	99.6*	75.7	57.5	62.3	83.0	67.8	68.7	57.9
MDTSI-FGSM _K	100.0*	80.2	63.4	66.2	87.3	67.1	69.6	55.4

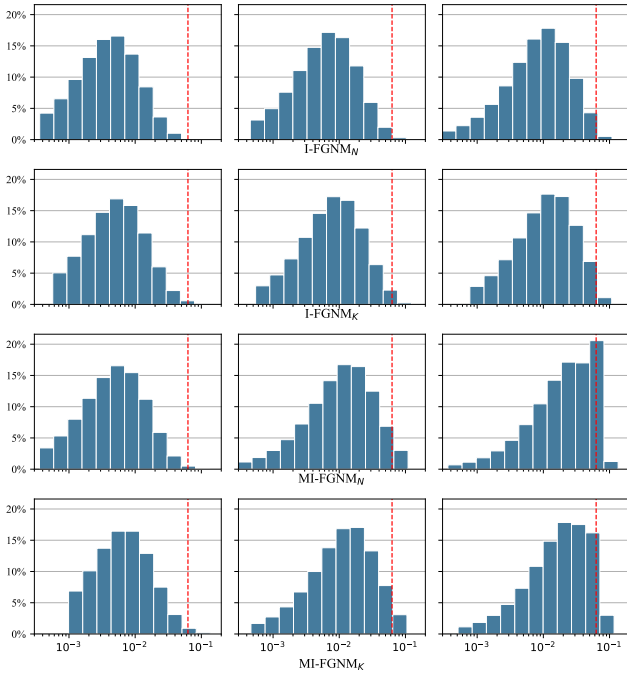


Figure 7: Histogram of absolute perturbations before clipping at iteration 2, 5, 10 with I-FGSM_N, I-FGSM_K, MI-FGSM_N and MI-FGSM_K, noises on the right side of the red dashed lines will be clipped. Compared to I-methods, MI-methods produces more perturbations to be clipped.

4.4.2 Visualization. To give qualitative analysis and confirm the effectiveness of generated perturbations, visualizations of adversarial examples are given. Specifically, we randomly choose several successful adversarial images for each approach, *i.e.*, I-FGSM, MI-FGSM, DI-FGSM, TI-BIM and SI-FGSM and plot the results in Figure 8. In this figure, the first row is the raw image while the remaining rows are adversarial examples crafted by original methods and ours FGSM_N and FGSM_K variants, respectively. As shown in the figure, noises are difficult to distinguish between original methods and ours visually. Notably, our FGSM_N variants produce nearly the same adversarial examples with originals, and FGSM_K variant slightly increases the noise level. The visualization indicates

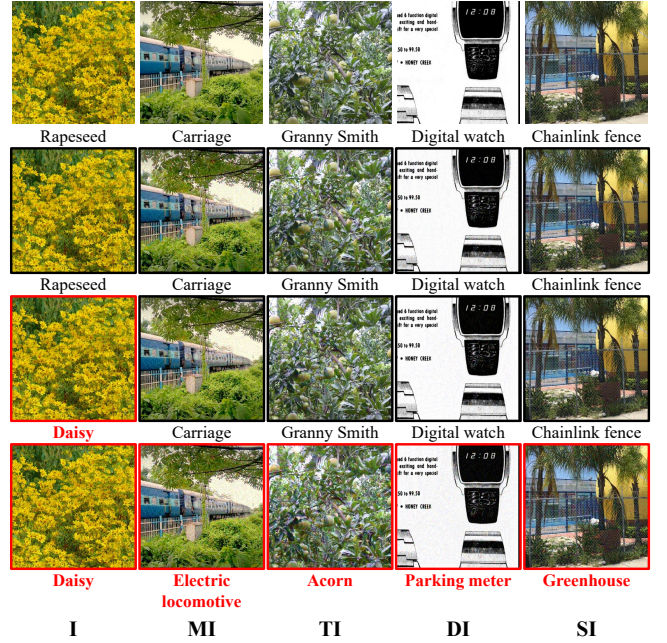


Figure 8: Visualization of adversarial examples. From top to bottom row-by-row: 1) raw images, 2) methods using sign operation, 3) methods with our fixed scale, *e.g.*, I-FGSM_N *etc.*, and 4) methods with our adaptive scale, *e.g.*, TI-BNIM_K *etc.*, where K is set to 12,000. From left to right are the basic algorithms adopted. We choose images generated by Inc-v3 white-box and tested on Inc-v4. The predictions are placed below the images, and mis-classified are highlighted in red.

our methods can easily gain a performance boost without adding significant noises.

4.5 Conclusion

Based on the Taylor expansion, we conduct a comprehensive analysis on the sign operation of gradient-based methods and reveal the gap between real gradients and resultant noises which leads to biased and inefficient attacks. To give a correction to this gap, a novel routine named Fast Gradient Non-sign Methods is proposed. Notably, FGSM is a general routine, which can seamlessly replace the conventional *sign* operation in gradient based attacks with negligible extra computational cost. To confirm the effectiveness of our FGSM, extensive experiments under the non-targeted ℓ_∞ attack settings are conducted. Significant performance gains are observed compared with state-of-the-art methods. Specifically, ours outperforms them by **27.5%** at most and **9.5%** on average.

REFERENCES

- [1] Wieland Brendel, Jonas Rauber, and Matthias Bethge. 2018. Decision-Based Adversarial Attacks: Reliable Attacks Against Black-Box Machine Learning Models. In *ICLR*.
- [2] Nicholas Carlini and David A. Wagner. 2017. Towards Evaluating the Robustness of Neural Networks. In *SP*.
- [3] Jianbo Chen, Michael I. Jordan, and Martin J. Wainwright. 2020. HopSkipJumpAttack: A Query-Efficient Decision-Based Attack. In *SP*.
- [4] Yanjie Chen, Likun Cai, Wei Cheng, and Hao Wang. 2020. Super-Resolution Coding Defense Against Adversarial Examples. In *MM*.
- [5] Xiaoyi Dong, Jiangfan Han, Dongdong Chen, Jiayang Liu, Huanyu Bian, Zehua Ma, Hongsheng Li, Xiaogang Wang, Weiming Zhang, and Nenghai Yu. 2020. Robust Superpixel-Guided Attentional Adversarial Attack. In *CVPR*.
- [6] Yinpeng Dong, Fangzhou Liao, Tianyu Pang, Hang Su, Jun Zhu, Xiaolin Hu, and Jianguo Li. 2018. Boosting adversarial attacks with momentum. In *CVPR*.
- [7] Yinpeng Dong, Tianyu Pang, Hang Su, and Jun Zhu. 2019. Evading defenses to transferable adversarial examples by translation-invariant attacks. In *CVPR*.
- [8] Xia Du, Chi-Man Pun, and Zheng Zhang. 2020. A Unified Framework for Detecting Audio Adversarial Examples. In *MM*.
- [9] Gintare Karolina Dziugaite, Zoubin Ghahramani, and Daniel M Roy. 2016. A study of the effect of jpg compression on adversarial images. *arXiv preprint arXiv:1608.00853* (2016).
- [10] Kevin Eykholt, Ivan Evtimov, Earlene Fernandes, Bo Li, Amir Rahmati, Chaowei Xiao, Atul Prakash, Tadayoshi Kohno, and Dawn Song. 2018. Robust physical-world attacks on deep learning visual classification. In *CVPR*.
- [11] Lianli Gao, Qilong Zhang, Jingkuan Song, Xianglong Liu, and Heng Tao Shen. 2020. Patch-wise attack for fooling deep neural network. In *ECCV*. Springer.
- [12] Ian J. Goodfellow, Jonathon Shlens, and Christian Szegedy. 2015. Explaining and Harnessing Adversarial Examples. In *ICLR*.
- [13] Chuan Guo, Mayank Rana, Moustapha Cissé, and Laurens van der Maaten. 2018. Countering Adversarial Images using Input Transformations. In *ICLR*.
- [14] Kaiming He, Xiangyu Zhang, Shaoqing Ren, and Jian Sun. 2016. Deep residual learning for image recognition. In *CVPR*.
- [15] Gao Huang, Zhuang Liu, Laurens Van Der Maaten, and Kilian Q Weinberger. 2017. Densely connected convolutional networks. In *CVPR*.
- [16] Jiayi Ji, Xiaoshuai Sun, Yiyi Zhou, Rongrong Ji, Fuhai Chen, Jianzhuang Liu, and Qi Tian. 2020. Attacking Image Captioning Towards Accuracy-Preserving Target Words Removal. In *MM*.
- [17] Stepan Komkov and Aleksandr Petiushko. 2019. Advhat: Real-world adversarial attack on arcface face id system. *arXiv preprint arXiv:1908.08705* (2019).
- [18] Zelun Kong, Junfeng Guo, Ang Li, and Cong Liu. 2020. PhysGAN: Generating Physical-World-Resilient Adversarial Examples for Autonomous Driving. In *CVPR*.
- [19] Deepak Kumar, Chetan Kumar, Chun-Wei Seah, Siyu Xia, and Ming Shao. 2020. Finding Achilles’ Heel: Adversarial Attack on Multi-modal Action Recognition. In *MM*.
- [20] Alexey Kurakin, Ian J. Goodfellow, and Samy Bengio. 2017. Adversarial examples in the physical world. In *ICLR*.
- [21] Maosen Li, Cheng Deng, Tengjiao Li, Junchi Yan, Xinbo Gao, and Heng Huang. 2020. Towards Transferable Targeted Attack. In *CVPR*.
- [22] Maosen Li, Cheng Deng, Tengjiao Li, Junchi Yan, Xinbo Gao, and Heng Huang. 2020. Towards Transferable Targeted Attack. In *CVPR*.
- [23] Ji Lin, Chuang Gan, and Song Han. 2019. Defensive Quantization: When Efficiency Meets Robustness. In *ICLR*.
- [24] Jiadong Lin, Chuankun Song, Kun He, Liwei Wang, and John E. Hopcroft. 2020. Nesterov Accelerated Gradient and Scale Invariance for Adversarial Attacks.
- [25] Aishan Liu, Jiakai Wang, Xianglong Liu, Bowen Cao, Chongzhi Zhang, and Hang Yu. 2020. Bias-based universal adversarial patch attack for automatic check-out. In *ECCV*.
- [26] Wenqing Liu, Miaojing Shi, Teddy Furon, and Li Li. 2020. Defending Adversarial Examples via DNN Bottleneck Reinforcement. In *MM*.
- [27] Yanpei Liu, Xinyun Chen, Chang Liu, and Dawn Song. 2017. Delving into Transferable Adversarial Examples and Black-box Attacks. In *ICLR*.
- [28] Yantao Lu, Yunhan Jia, Jianyu Wang, Bai Li, Weiheng Chai, Lawrence Carin, and Senem Velipasalar. 2020. Enhancing Cross-Task Black-Box Transferability of Adversarial Examples With Dispersion Reduction. In *CVPR*.
- [29] Chengcheng Ma, Weiliang Meng, Baoyuan Wu, Shibao Xu, and Xiaopeng Zhang. 2020. Efficient Joint Gradient Based Attack Against SOR Defense for 3D Point Cloud Classification. In *MM*.
- [30] Chen Ma, Chenxu Zhao, Hailin Shi, Li Chen, Jun-Hai Yong, and Dan Zeng. 2019. MetaAdvDet: Towards Robust Detection of Evolving Adversarial Attacks. In *MM*.
- [31] Aleksander Madry, Aleksandar Makelov, Ludwig Schmidt, Dimitris Tsipras, and Adrian Vladu. 2018. Towards Deep Learning Models Resistant to Adversarial Attacks. In *ICLR*.
- [32] Seyed-Mohsen Moosavi-Dezfooli, Alhussein Fawzi, and Pascal Frossard. 2016. DeepFool: A Simple and Accurate Method to Fool Deep Neural Networks. In *CVPR*.
- [33] Nicolas Papernot, Patrick D. McDaniel, Ian J. Goodfellow, Somesh Jha, Z. Berkay Celik, and Ananthram Swami. 2017. Practical Black-Box Attacks against Machine Learning. In *AsiaCCS*.
- [34] Mahmood Sharif, Sruti Bhagavatula, Lujo Bauer, and Michael K Reiter. 2016. Accessorize to a crime: Real and stealthy attacks on state-of-the-art face recognition. In *CCS*.
- [35] Mahmood Sharif, Sruti Bhagavatula, Lujo Bauer, and Michael K. Reiter. 2016. Accessorize to a Crime: Real and Stealthy Attacks on State-of-the-Art Face Recognition. In *CCS*.
- [36] Christian Szegedy, Sergey Ioffe, Vincent Vanhoucke, and Alexander Alemi. 2017. Inception-v4, inception-resnet and the impact of residual connections on learning. In *AAAI*.
- [37] Christian Szegedy, Sergey Ioffe, Vincent Vanhoucke, and Alexander Alemi. 2017. Inception-v4, inception-resnet and the impact of residual connections on learning. In *AAAI*.
- [38] Christian Szegedy, Vincent Vanhoucke, Sergey Ioffe, Jon Shlens, and Zbigniew Wojna. 2016. Rethinking the inception architecture for computer vision. In *CVPR*.
- [39] Florian Tramèr, Alexey Kurakin, Nicolas Papernot, Ian J. Goodfellow, Dan Boneh, and Patrick D. McDaniel. 2018. Ensemble Adversarial Training: Attacks and Defenses. In *ICLR*.
- [40] Florian Tramèr, Alexey Kurakin, Nicolas Papernot, Ian J. Goodfellow, Dan Boneh, and Patrick D. McDaniel. 2018. Ensemble Adversarial Training: Attacks and Defenses. In *ICLR*.
- [41] Run Wang, Felix Juefei-Xu, Qing Guo, Yihao Huang, Xiaofei Xie, Lei Ma, and Yang Liu. 2020. Amora: Black-box Adversarial Morphing Attack. In *MM*.
- [42] Weibin Wu, Yuxin Su, Xixian Chen, Shenglin Zhao, Irwin King, Michael R. Lyu, and Yu-Wing Tai. 2020. Boosting the Transferability of Adversarial Samples via Attention. In *CVPR*.
- [43] Cihang Xie, Zhishuai Zhang, Yuyin Zhou, Song Bai, Jianyu Wang, Zhou Ren, and Alan L Yuille. 2019. Improving transferability of adversarial examples with input diversity. In *CVPR*.
- [44] Bin Yan, Dong Wang, Huchuan Lu, and Xiaoyun Yang. 2020. Cooling-Shrinking Attack: Blinding the Tracker With Imperceptible Noises. In *CVPR*.
- [45] Minghao Yin, Yongbing Zhang, Xiu Li, and Shiqi Wang. 2018. When Deep Fool Meets Deep Prior: Adversarial Attack on Super-Resolution Network. In *MM*.